SCISPACE
formerly Typeset

Open access • Journal Article • DOI:10.1021/LA904840Q

Quantification of Thin Film Crystallographic Orientation Using X-ray Diffraction with an Area Detector — Source link

Jessica L. Baker, Leslie H. Jimison, Stefan C. B. Mannsfeld, Steven K. Volkman ...+5 more authors

Institutions: University of California, Berkeley, Stanford University

Published on: 02 Apr 2010 - Langmuir (American Chemical Society)

Topics: Texture (crystalline), Thin film, Microelectronics and Pole figure

Related papers:

- Quantitative determination of organic semiconductor microstructure from the molecular to device scale.
- Two-dimensional charge transport in self-organized, high-mobility conjugated polymers
- Highly oriented crystals at the buried interface in polythiophene thin-film transistors
- A general relationship between disorder, aggregation and charge transport in conjugated polymers
- Effects of Thermal Annealing Upon the Morphology of Polymer-Fullerene Blends

Share this paper:

View more about this paper here: https://typeset.io/papers/quantification-of-thin-film-crystallographic-orientation-52ck58rikq

Quantification of thin film crystallographic orientation using X-ray diffraction with an area detector

Jessy L Baker[1], Leslie H Jimison[4], Stefan Mannsfeld[5], Steven Volkman[3], Shong Yin[3], Vivek Subramanian[3], Alberto Salleo[4], A Paul Alivisatos[2], Michael F Toney[5]

[1]Department of Mechanical Engineering
[2]Department of Chemistry
[3]Department of Electrical Engineering and Computer Sciences
University of California, Berkeley, Berkeley, California 94720

[4]Department of Materials Science and Engineering, Stanford University, Stanford, California 94305
[5]Stanford Synchrotron Radiation Lightsource, Menlo Park, California 94025

As thin films become increasingly popular (for solar cells, LEDs, microelectronics, batteries), quantitative morphological and crystallographic information is needed to predict and optimize the film's electronic, optical and mechanical properties. This quantification can be obtained quickly and easily with X-ray diffraction using an area detector in two simple sample geometries. In this paper, we describe a methodology for constructing complete pole figures for thin films with fiber texture (isotropic in-plane orientation). We demonstrate this technique on semicrystalline polymer films, self-assembled nanoparticle semiconductor films, and randomly-packed metallic nanoparticle films. This method can be immediately implemented to help

understand the relationship between film processing and microstructure, enabling the development of better and less expensive electronic and optoelectronic devices.

Keywords: grazing-incidence X-ray diffraction; pole figure; texture analysis; morphology; thin film

Introduction

The optical and electronic properties of polycrystalline and semicrystalline materials are highly dependent on the materials' morphology. When these properties are anisotropic in the single crystal form, the corresponding bulk properties of the poly- or semi-crystalline material are often dependent upon the orientation distribution of the crystallites.[1] As efforts are made to optimize the electrical and optical properties of functional, solution-processed polycrystalline films used for thin film transistors, solar cells, and other emerging technologies, it is necessary to fully characterize the orientation distribution, or texture, of the crystallites. There has been much effort devoted to correlating the microstructure and properties of thin films (<100 nm) of nanostructured organic semiconductors [2-7] and inorganic semiconducting nanoparticles[8, 9], but the collection of complete texture information is often challenging due to the limited film thickness. In this work, we introduce an X-ray diffraction-based method for collecting and constructing quantitative pole figures with an area detector for thin films with isotropic crystallographic orientation in the substrate plane (classically referred to as fiber texture). The technique is rapid and ideal for thin films that are sensitive to beam damage, diffract weakly or are otherwise limited by their thin film form to certain diffraction geometries.

A pole figure is a plot of the orientation distribution of a particular set of crystallographic lattice planes, providing a useful illustration of a material's texture. Traditional pole figures of bulk samples can be collected in either reflection or transmission mode. Pole figures collected in a reflection mode utilize a symmetric geometry introduced by Schultz [10-12]. In this technique, diffraction intensities are collected using a point detector as the sample is rotated along two axes. Accurate collection of intensity in the Schultz geometry is generally limited to within 85° of the surface normal, due to distortions that arise at the substrate edge. Transmission techniques [13-15] are feasible, but require either intensity corrections or special sample shapes, and in general cannot be used for thin films for which the substrate absorbs the X-rays. Whether dealing with reflection or transmission geometries, collection with a point detector across such a large slice of the reciprocal lattice space is time-intensive, especially for thin films. The use of an area detector facilitates more rapid collection of intensity across a large section of reciprocal space, greatly decreasing total acquisition time. Area detectors are commonly used with transmission-based geometries, allowing for the simultaneous collection of Debye-Scherrer rings from multiple Bragg reflections[16, 17]. The use of flat area detectors in combination with reflection geometries for thin films results in some image distortions, making quantitative analysis difficult. Many research groups have reported useful, but mostly only qualitative, texture data of delicate thin films collected using grazing incidence synchrotron radiation with an area detector [5, 8, 18-24].

In the work presented here, we perform the diffraction experiments with a synchrotron radiation light source. The high photon flux of synchrotron radiation allows for efficient diffraction measurements of materials whose low crystal symmetry, small scattering cross section, or high beam sensitivity limits the characterization that is possible with an in house, lab-based source due to low signal to noise ratios[25]. Even for samples for which the aforementioned

limitations do not apply, the use of high flux synchrotron radiation greatly reduces collection time required, and together with the use of an area detector allows for rapid pole figure collection (minutes rather than hours)[26, 27]. This is becoming a widespread method to collect texture data, and some software has been developed to calculate pole figures from Debye-Scherrer rings collected in transmission[17].

Few pole figures of thin solution-processed films have been published in the literature. These films often require the support of a rigid substrate and thus cannot be used for transmission-based diffraction geometries. The weak diffraction often associated with thin solution-cast films further contribute to the difficultly of pole figure data collection. The organic films used for published pole figures are typically limited to thick films on the order of microns[11, 28, 29] or otherwise highly diffracting materials[30], while functional organic semiconductors are applied as thin films less than ~100 nm, and often diffract weakly (especially semiconducting polymers). Thin films can have a crystal structure different from the bulk material as well as distinct texture. Published pole figures collected from solution-processed thin films of inorganic nanoparticles are also limited, due in large part to weak diffraction. Korgel and coworkers have collected small-angle scattering data of organized spherical particles[18-20], but similar small-angle work has not been performed on anisotropic nanoparticles. Breiby et al.[8] have published plots representing the orientation distribution of CdS nanorods in the plane of the substrate, taking advantage of the large beam footprint and interface sensitivity in wide-angle grazing incidence geometry. However, complete pole figures (biaxial in this case) were not reported and the orientation of nanorods out of the plane of the substrate was found using a model-dependent fit. The ideal pole figure collection technique for texture analysis must be both time efficient and capable of measuring the entire span of crystallite orientations: polar angles, χ, from -90^{o} to 90^{o} (see Figure

1 for an illustration of diffraction geometry; we assume that the sample is approximately horizontal throughout this paper). The goal of this paper is to elucidate an efficient methodology for the construction of such pole figures for fiber textured thin films. Although we chose to work with synchrotron radiation for time-efficiency, high signal-to-noise ratios, and sample lifetime considerations, this discussion could be applied to diffraction collected with an area detector and an in house, lab-based source, provided the polarization correction was modified according to the source used[31].

Obtaining a complete, accurate thin-film pole figure

We present a method of pole figure compilation for thin films with a fiber texture, where the crystallite orientation distribution is isotropic in the plane of the substrate, using synchrotron radiation and an area detector. This involves two separate measurements: one in grazing incidence geometry and one with the geometry locally satisfying the specular condition. Using a grazing incidence X-ray beam for diffraction greatly increases the signal to noise ratio by increasing the X-ray path length through the film, allowing for accurate intensity collection from weakly diffracting samples. The large beam footprint also serves to spread the beam power across the sample, resulting in less destructive data collection for radiation sensitive samples. However, raw intensity collected with a flat detector in grazing incidence geometry is distorted[32], and the detector image is not a direct map of reciprocal space. This makes it difficult to extract quantitative texture information. By appropriately combining intensity extracted from grazing incidence diffraction patterns with intensity extracted from local-specular diffraction patterns (where the proper choice of incidence angle prevents distortion near the Bragg reflection at hand), we obtain complete pole figures that represent the true intensity of a Bragg reflection

across the entire span of polar angle χ (-90^o to 90^o). This technique is simple, efficient and applicable to any thin film with a fiber texture. The only intensity corrections needed are for polarization and X-ray absorption (which is often negligible for thin films). This method can be immediately implemented to better understand the relationship between film processing and microstructure, enabling the development of solution-processed and inexpensive electronic and optoelectronic devices.

The assumptions made in this work are that (a) the sample has an isotropic crystallite orientation distribution in the plane of the substrate (i.e., has a fiber texture), or fiber texture is artificially created by rotating the substrate normal throughout the measurement, (b) the film thickness to be probed does not exceed ~100 nm (with a more exact thickness requirement depending up on the incidence angle as well as the material in question[33]) and (c) the detector sensitivity is not polarization-dependent. The geometry of the diffraction setup used in this work is detailed in Figure 1. Throughout our data analysis, we work with Bragg reflections corresponding to one chosen lattice spacing with Bragg angle $\boldsymbol{\theta_B}$ and reciprocal lattice vector $\mathbf{q}_B$. The Bragg reflections chosen for analysis have strong intensities, giving high signal-to-noise ratios. If possible, strong peaks that are far from the beamstop, and thus affected less by the air scattering background, are preferable. Software is used to extract the Bragg peak intensities as a function of polar angle $\boldsymbol{\chi}$, where $\boldsymbol{\chi} = 0$ coincides with the $\mathbf{q}_z$ axis (see Supporting Information). To achieve this, intensity is extracted along an annular region encompassing $\mathbf{q}_B$ and appropriate background subtractions are made.

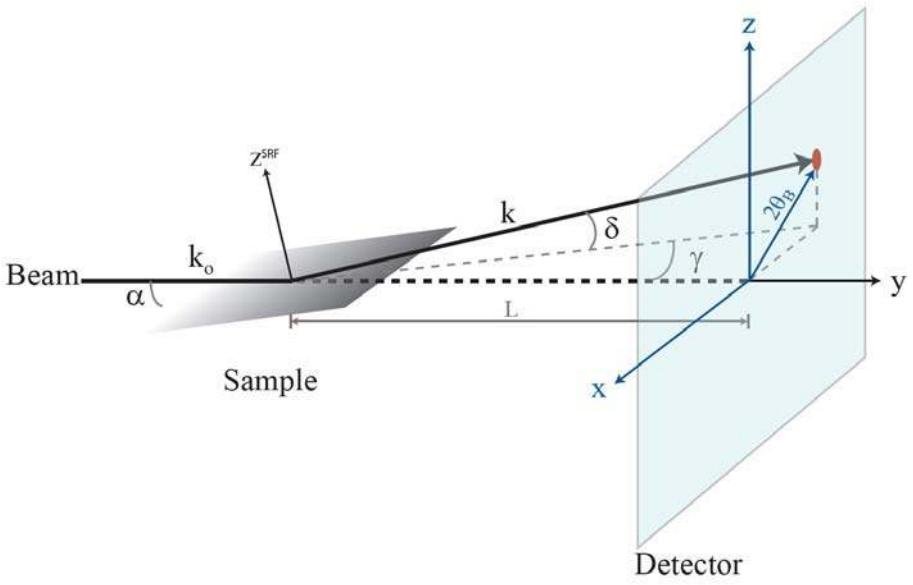

Figure 1. Schematic of diffraction measurement setup, including relevant geometry definitions. We assume that the sample is approximately horizontal throughout this paper. α is the angle of sample tilt (with respect to the incoming beam), z^{srf} is the sample surface normal of the sample, k_o is the incoming radiation wavevector, k is the outgoing (diffracted) radiation wavevector, L is the detector-sample distance, δ is the vertical angle (with respect to the incoming beam) of the diffracted beam, γ is the horizontal angle (with respect to the incoming beam) of the diffracted beam, x and z are the planar coordinates of the area detector, and θ_B is the Bragg angle.

2.1 χ-Correction

Images collected with a grazing incidence geometry and a flat area detector are useful for qualitative analysis, but are not reciprocal space maps. To understand the distortions caused by the flat detector and grazing incidence geometry, it is helpful to imagine a sphere of crystallite orientations in reciprocal space. The radius of this orientation sphere is defined by the $\mathbf{q_B}$ of interest. The center of this sphere corresponds to **q**=0 and is placed on the surface of the Ewald sphere at the head of the incoming **k** vector (See Fig 2). From this construction, we can see the intersection of these two spheres, corresponding to all observable diffraction in this geometry.

This figure illustrates the importance of working with a sample that is either isotropic in-plane or rotated about z^{SRF} (sample surface normal) throughout the measurement (effectively creating in-plane isotropy). Crystallites with $\mathbf{q_B}$ near in-plane (Fig 2, vector ***a***) will intersect the Ewald sphere, while those with $\mathbf{q_B}$ close to perpendicular (Fig 2, vector ***b***) will not intersect the Ewald sphere and thus do not result in observed diffraction. The most vertical orientation that will result in observed diffraction (corresponding to the minimum detectable χ) has a polar angle of θ_B (Fig 2, vector c). In other words, rather than ranging [-90 ^{o} to 0 ^{o} to 90^o], χ is constrained to a range of [-90^o to -θ_B ^{o} and θ_B ^{o} to 90 ^{o}] in the grazing incidence geometry. Thus, the intensity displayed along a vertical slice of the detector through the beamstop arises from crystallites with χ near θ_B. Interpretation of this vertical slice as the specular diffraction is thus incorrect, as has been pointed out previously[32, 34]. With this in mind, we collect intensity using an area detector in the grazing incidence geometry, assuring that the incidence angle used is above the critical angle for total external reflection to probe the entire film thickness. From the two dimensional pattern, we extract intensity as a function of χ along an arc with radius q_B. The arc used to extract intensity has a width Δq that is chosen to encompass the entire peak. Appropriate background subtractions are made to assure that collected intensity arises from diffraction from the crystallites and not extraneous scattering. This data set serves as the starting point for pole figure compilation, with the understanding that the signal near χ=**0** is distorted and is not the true intensity.

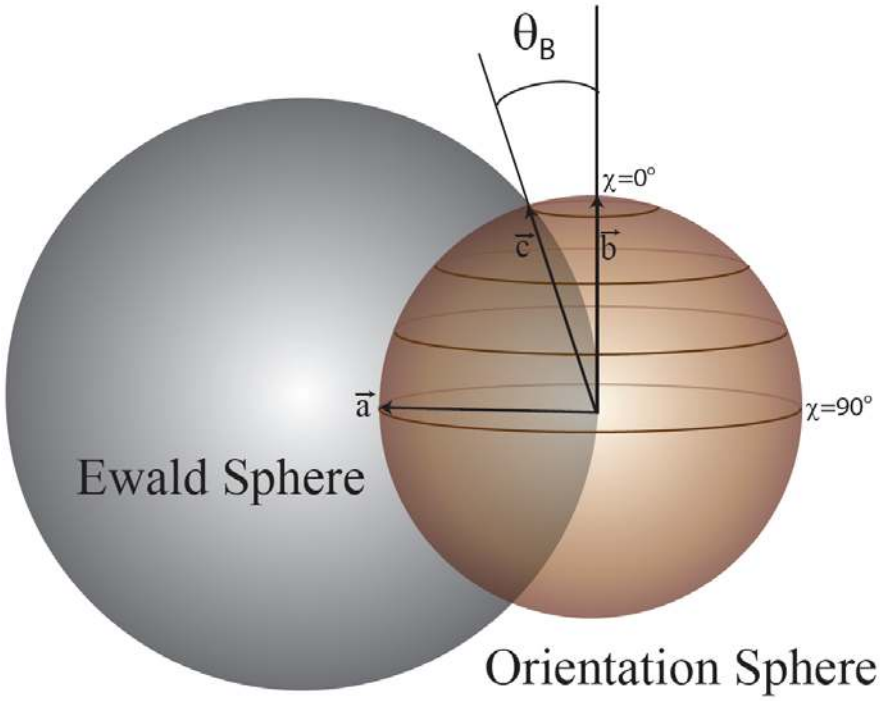

Figure 2. Intersection of Ewald sphere with crystallite orientation sphere, indicating possible diffraction events in grazing incidence geometry. **a** is the vector denoting an in-plane reciprocal lattice vector that results in pure horizontal scattering ($\chi = 90^{o}$), **b** is the vector denoting an out-of-plane reciprocal lattice vector ($\chi = 0^{o}$), which in the grazing-incidence geometry does not result in any observable scattering, and **c** is the vector denoting off-vertical reciprocal lattice vector which results in pure vertical scattering in the grazing incidence diffraction geometry. The local-specular condition is met when the substrate (and therefore orientation sphere) is tilted at θ_B.

To amend this distortion and move toward a complete pole figure, an additional data set is extracted from a second two-dimensional diffraction pattern, taken with the substrate tilted at an incident angle $\alpha = \theta_B$, such that the pole of the orientation sphere of the Bragg peak intersects the Ewald sphere. We refer to these curves as "local-specular," because of the exact satisfaction of the specular condition near the Bragg peak of interest. This type of scan has been referred to previously as a 'wide-angle rocking curve', since the substrate is rocked into the specular condition[21, 24]). We compile the full pole figure by appropriately merging the [intensity, χ] data

sets extracted from the local-specular diffraction pattern and the grazing incidence diffraction pattern. To determine an appropriate merging angle for these two data sets, we plot intensity vs. χ for both diffraction patterns and adjust the arbitrary amplitude of one curve until both curves overlay (i.e. their local derivatives are identical) within the appropriate angular bounds. The relevant angular range for local-specular data is $\mathbf{0^o} > \chi > \mathbf{60^o}$, while the relevant angular range for grazing data is $\theta_B < \chi < \mathbf{90^o}$. The θ_B bound arises from the intersection of the Ewald and orientation sphere in grazing incidence geometry (see above), and the $\mathbf{60^o}$ bound arises from the physical blocking of the horizon diffraction by the substrate edge after tilting into Bragg condition in the local-specular geometry (See Supporting Information for geometrical expression). The value between θ_B and $\mathbf{60^o}$ at which the two sets of data are merged is operationally determined by the signal to noise ratio in the data.

A Lorentz correction [36-38] is required in X-ray geometries that involves either a rotating single crystal or a stationary powder sample. However, in the present case of morphology quantification (as opposed to structural characterization) the data are obtained from a single Bragg ring, which obviates the need for a Lorentz correction.

2.2 Polarization Correction

Synchrotron radiation is horizontally polarized, causing diffraction intensities which vary with angle.[31]. To correct for this, we divide collected intensity by the polarization correction factor given in Eq. 1[36, 39]:

$$C_p = p_h\left(1-\cos^2\delta\cdot\sin^2\gamma\right)+\left(1-p_h\right)\cdot\left(1-\sin^2\delta\right) \qquad \text{Eq. 1}$$

Here p_h is the fraction of radiation that is polarized in the horizontal direction (typically about 98% for a synchrotron source) and the angles δ and γ correspond to geometry shown in Figure 1.

2.3 Absorbance Correction

The path an X-ray follows through a film is longer at low exit angles than at high angles. If the absorbance of the film is high, this can affect the diffraction intensity data. Assuming a uniform sample absorbance, the expression for the correction is[40, 41]:

$$C_a = \frac{1 - e^{-\mu \cdot t\left(\frac{1}{\sin(\alpha)} + \frac{1}{\sin(\delta)}\right)}}{\mu \cdot \left(\frac{1}{\sin(\alpha)} + \frac{1}{\sin(\delta)}\right)} \quad , \qquad \text{Eqn. 2}$$

where μ is the extinction coefficient (or inverse of the penetration depth at low angles) and t is the film thickness. Note that in many films, this correction is negligibly small. We can express the total intensity correction factor as the product of equations (1) and (2): $C_f = Cp * Ca$.

In summary, we collect two diffraction patterns for each sample: one at grazing incidence and one at an incidence angle satisfying the specular condition. Detector coordinates [x, z] are converted to angles γ and δ, θ_B and χ. This image is used to obtain the intensity versus χ through an annular region at a selected Bragg ring, and any background intensity present is subtracted. The I(χ) data are corrected for polarization and absorption. The two I(χ) figures are scaled and merged at an angle greater than θ_B but less than an upper bound angle, $\mathbf{60^o}$, defined by diffraction geometry; the intensity nearest the pole consists of data collected from the local specular diffraction pattern, while the intensity at larger angles of χ corresponds to the diffraction pattern taken at grazing incidence. On the completion of a satisfactory merge, we obtain our final,

complete pole figure. The data analysis for this technique can be carried out quickly using WxDiff software [32].

Some experimental results & technique application

Examples of materials for which this pole figure technique can be readily applied include thin films of nanostructured organic and inorganic semiconductors and nanostructured metallic thin films. For the semiconductors in particular, films are often fabricated via solution processing techniques such as printing, painting, or spray coating. It is useful to be able to quantify crystallite orientation distributions across these multi-parameter film deposition techniques. Diffraction data and intensity-corrected pole figures for three sample systems are plotted in Figure 3. These data were obtained on SSRL beam line 11-3 with a MAR345 image plate detector and an X-ray energy of 12.7 keV. For the grazing angle data, the vertical incident beam size was 0.05 mm, and the incidence angles were above the critical angles for the film examined (0.12^{o} for polymer, 0.15^{o} for both CdS and Au films). For the local specular data, the vertical incident beam size was 0.15 mm (full beam height). The q and Δq values we chose for integration $q \cong .725$ Å^{-1} and $\Delta q = 0.15$ Å^{-1} (polymer); $q \cong 1.865$ Å^{-1} and $\Delta q = 0.07$ Å^{-1} (CdS); $q \cong 2.7$ Å^{-1} and $\Delta q = 0.14$ Å^{-1} (Au).

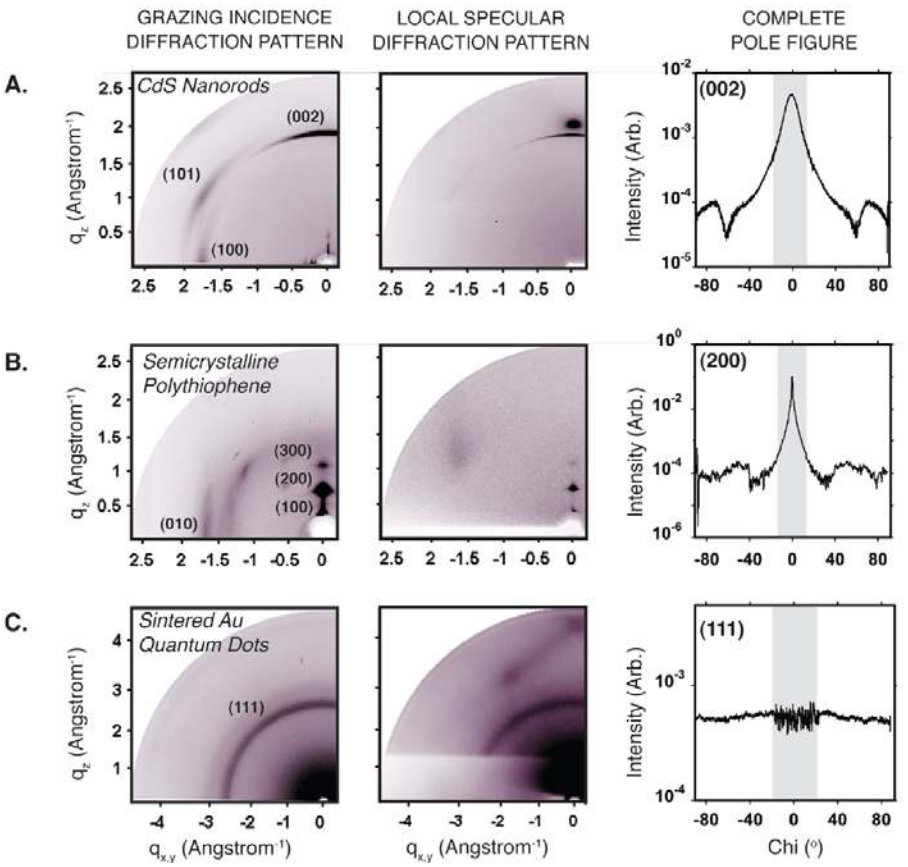

Figure 3. Example data for three different materials: A) CdS nanorods deposited by slow evaporation of nanorod solution, B) semicrystalline polymer poly[5,5'-bis(3-dodecyl-2-thienyl)-2,2'-bithiophene] (PQT-12) deposited by spin-casting, and C) sintered Au quantum dots deposited by spin-casting. The column on the left shows diffraction patterns collected in grazing incidence geometry. The middle column shows diffraction patterns taken with specular condition satisfied for the desired Bragg reflection, referred to as local-specular. The column on the right shows the complete pole figure, compiled by appropriately combining data from the grazing incidence diffraction patterns (unshaded regions) and the specular diffraction patterns (shaded region.) The specular diffraction patterns are necessary to complete the pole figures: the intensity highlighted in grey is not probed in the grazing incidence geometry and is instead collected in the local specular curves. Note that the intensity shown along $q_{xy}= 0$ in the grazing incidence images is distorted as described above (e.g., are not truly at $q_{xy} = 0$) but images are shown in this fashion for simplicity.

In a film composed of rod-shaped cadmium sulfide nanoparticles (Fig 3A), electron mobility normal to the film (and therefore device performance) can be improved by vertically orienting the nanorods, making the through-film direction appear as single-crystalline. Such a film of vertically aligned nanorods could offer high performance solar cells or LEDs at a low (solution-processed) cost. Our texture analysis method can be used to quantify the degree of vertical orientation in each film, thus allowing optimization of the nanorod deposition process[9]. Strong texture can be observed from both the grazing incidence and local specular diffraction patterns of the film in Figure 3a. The (002) reflection appears with the strongest signal, and corresponds to the long axis of the wurtzite nanorod. The (101) and (100) reflections can also be observed, with angles appropriate for these respective crystal directions in reciprocal space. In principal, any of these reflections could be used to construct a pole figure, but with a lower signal to noise ratio for the (101) and (100). We construct a pole figure by correcting and merging these two diffraction patterns, using the (002) reflection because of its strong intensity. We see a strong preference for vertical (χ=0) orientation of the (002) wurtzite crystal direction (long axis of nanorod), which indicates we have found appropriate processing conditions for our desired film of vertically aligned nanorods.

The electronic performance, namely the field-effect mobility, of thin films of polymer semiconductors has a similar dependence on film microstructure. Semicrystalline semiconducting polymers generally form films with crystallites on the order of 10-15 nm in diameter that are isotropically oriented in the plane of the substrate, with various degrees of ordering in the out of plane direction[3, 21, 23, 24]. The film texture depends strongly on the processing conditions. In the grazing incidence X-ray scattering pattern shown, we see three strong (h00) peaks, which arise from the backbone stacking of the polymers in the direction

perpendicular to the substrate. The (010), arising from cofacial molecular stacking in the plane of the substrate, is visible along the horizon of the grazing incidence pattern. For this sample, we chose to compile a pole figure based on the (200) Bragg reflection (because of its strong intensity and distance from the direct beam). From the two diffraction patterns, we constructed a complete pole figure for the (200) Bragg reflection that confirms a strong tendency for out-of-plane texture. By quantifying the orientation distribution using (h00) pole figures, we can indirectly obtain information concerning the misorientation between neighboring crystallites. By comparing pole figures of multiple samples, we can more effectively study how microstructure (and in turn charge transport) changes with processing conditions. The complete pole figures shown in Figure 3b play an important role in film optimization.

In the case of the gold nanoparticle film, the goal was to understand the transformation of discrete particles into continuous metal films. Mechanically stable films can be formed from these particles at temperatures as low as 120 °C, with 70% the conductivity of bulk gold[43]. The texture of these metal films varies with sintering condition, though in the case of gold films, highly textured films are generally not seen. This is not the case for other metal systems such as silver where both (111) textured and untextured films can be produced depending on processing conditions. Because different crystal planes have different work functions, film texture will change the effective film work function. Also in the formation of microelectronic mechanical systems (MEMS), such as cantilevers, the mechanical properties of the films are drastically affected by the orientation of the metal films[44]. Both the diffraction pattern and the pole figure indicate almost no preference in orientation of the gold nanocrystals for this sintering condition, making this a useful control for probing film texture. Note that the data from the local specular

condition is much noisier than the grazing data, due to the lower signal that results from a smaller sampling area.

The examples included in this discussion (the semiconducting nanoparticle film, the nanostructured semicrystalline semiconducting polymer and the sintered gold nanoparticle film) were chosen to illustrate the broad range of our method's utility. This method can be applied to any diffracting thin films with fiber texture. In the cases mentioned, complete pole figures have been a critical tool for the characterization of film structure, giving insight into the effect of various processing conditions.

Conclusion

We have demonstrated a fast and efficient data collection technique using synchrotron radiation and a flat area detector for the characterization of crystallographic orientation for functional thin films, and outlined a method for quantifying film texture by merging two, corrected data sets. In this work, we bring attention to inherent distortions in intensity collected using a flat image plate and discuss the correct factors and data merging techniques needed to use the data in a quantitative manner. The method presented here can serve as a valuable tool in the optimization of microstructure-dependent performance.

Acknowledgements

This work was funded by the Helios Solar Energy Research Center, which is supported by the Director, Office of Science, Office of Basic Energy Sciences, Materials Sciences and Engineering Division, of the U.S. Department of Energy under Contract No. DE-AC02-05CH11231. Portions of this research were carried out at the Stanford Synchrotron Radiation

Lightsource, a national user facility operated by Stanford University on behalf of the U.S. Department of Energy, Office of Basic Energy Sciences. We gratefully acknowledge financial support from the National Science Foundation in the form of a Career Award (AS) and Graduate Student Fellowship Personnel expenses (JLB, LHJ).

References

1. Robert L. Snyder, J. F., Hans L. Bunge *Defect and Microstructure Analysis by Diffraction*. Oxford University Press: Oxford, **1999**.
2. Jimison, L. H.; Toney, M. F.; Mcculloch, I.; Heeney, M.; Salleo, A., Charge-Transport Anisotropy Due to Grain Boundaries in Directionally Crystallized Thin Films of Regioregular Poly(3-hexylthiophene). *Adv. Mater.* **2009**.
3. Kline, R.; McGehee, M.; Kadnikova, E.; Liu, J.; Frechet, J.; Toney, M., Dependence of regioregular poly(3-hexylthiophene) film morphology and field-effect mobility on molecular weight. *Macromolecules* **2005,** 38, (8), 3312-3319.
4. Joseph Kline, R.; Mcgehee, M. D.; Toney, M. F., Highly oriented crystals at the buried interface in polythiophene thin-film transistors. *Nat Mater* **2006,** 5, (3), 222-228.
5. Breiby, D. W.; Sa, u., E. J., Quantification of preferential orientation in conjugated polymers using X-ray diffraction. *J. Polym. Sci. B Polym. Phys.* **2003,** 41, (20).
6. Resel, R.; Ottmar, M.; Hanack, M.; Keckes, J.; Leising, G., Preferred orientation of copper phthalocyanine thin films evaporated on amorphous substrates. *J Mater Res* **2000,** 15, (4), 934-939.
7. Kline, J. R.; Mcgehee, M. D.; Toney, M. F., Highly oriented crystals at the buried interface in polythiophene thin-film transistors. *Nat Mater* **2006,** 5, (3), 222-228.
8. Breiby, D.; Chin, P.; Andreasen, J., Biaxially Oriented CdSe Nanorods. *Langmuir* **2009,** 25, (18), 10970-10974.
9. Baker, J. L.; Widmer-Cooper, A.; Toney, M. F.; Geissler, P. L.; Alivisatos, A. P., Device-Scale Perpendicular Alignment of Colloidal Nanorods. *Nano Letters* **2010**.
10. Schulz, L., A direct method of determining preferred orientation of a flat reflection sample using a Geiger counter X-ray spectrometer. *J. Appl. Phys.* **1949,** 20, 1030.
11. Gilbert, M.; Ross, D.; Bowen, A., X-ray pole figures for oriented PVC. *Polymer(Guildford)* **1999,** 40, (5), 1233-1239.
12. You, L.; Yang, G.; Knorr, D.; McDonald, J.; Lu, T., Texture of vapor deposited parylene thin films. *Appl. Phys. Lett.* **1994,** 64, 2812.
13. Decker, B.; Asp, E.; Harker, D., Preferred Orientation Determination Using a Geiger Counter X-ray Diffraction Goniometer. *J. Appl. Phys.* **1948,** 19, (4), 388-392.
14. Norton, J., A Technique for Quantitative Determination of Texture of Sheet Metals. *J. Appl. Phys.* **1948,** 19, (12), 1176-1178.
15. Schwartz, M., … for Obtaining Complete Quantitative Pole Figures for Flat Sheets Using One Sample and …. *J. Appl. Phys.* **1955**.

16. Rodriguez-Navarro, A. B., Registering pole figures using an X-ray single-crystal diffractometer equipped with an area detector. *J Appl Crystallogr* **2007,** 40, (3), 631-634.
17. Garbe, U., New pole figure calculation software: 2DiffCalc. *J Appl Crystallogr* **2009,** 42, (4), 730-733.
18. Korgel, B. A.; Fullam, S.; Connolly, S.; Fitzmaurice, D., Assembly and Self-Organization of Silver Nanocrystal Superlattices: Ordered "Soft Spheres". *The Journal of Physical Chemistry B* **1998,** 102, (43), 8379-8388.
19. Connolly, S.; Fullam, S.; Korgel, B.; Fitzmaurice, D., Time-Resolved Small-Angle X-ray Scattering Studies of Nanocrystal Superlattice Self-Assembly. *Journal of the American Chemical Society* **1998,** 120, (12), 2969-2970.
20. Korgel, B. A.; Fitzmaurice, D., Small-angle x-ray-scattering study of silver-nanocrystal disorder-order phase transitions. *Physical Review B* **1999,** 59, (22), 14191.
21. Jimison, L. H.; Salleo, A.; Chabinyc, M. L.; Bernstein, D. P.; Toney, M. F., Correlating the microstructure of thin films of poly[5,5-bis(3-dodecyl-2-thienyl)-2,2-bithiophene] with charge transport: Effect of dielectric surface energy and thermal annealing. *Physical Review B* **2008,** 78, (12), -.
22. Belman, N.; Acharya, S.; Konovalov, O.; Vorobiev, A.; Israelachvili, J.; Efrima, S.; Golan, Y., Hierarchical Assembly of Ultranarrow Alkylamine-Coated ZnS Nanorods: A Synchrotron Surface X-Ray Diffraction Study. *Nano Lett* **2008,** 8, (11), 3858-3864.
23. Sirringhaus, H.; Brown, P. J.; Friend, R. H.; Nielsen, M. M.; Bechgaard, K.; Langeveld-Voss, B. M. W.; Spiering, A. J. H.; Janssen, R. A. J.; Meijer, E. W.; Herwig, P.; de Leeuw, D. M., Two-dimensional charge transport in self-organized, high-mobility conjugated polymers. *Nature* **1999,** 401, (6754), 685-688.
24. Chabinyc, M. L.; Toney, M. F.; Kline, R. J.; Mcculloch, I.; Heeney, M., X-ray scattering study of thin films of poly(2,5-bis(3-alkylthiophen-2-yl)thieno[3,2-b]thiophene). *J Am Chem Soc* **2007,** 129, (11), 3226-3237.
25. Wcislak, L.; Klein, H.; Bunge, H.; Garbe, U.; Tschentscher, T.; Schneider, J., Texture analysis with high-energy synchrotron radiation. *J Appl Crystallogr* **2002,** 35, 82-95.
26. Wenk, H.; Grigull, S., Synchrotron texture analysis with area detectors. *J Appl Crystallogr* **2003,** 36, 1040-1049.
27. Heidelbach, F.; Riekel, C.; Wenk, H., Quantitative texture analysis of small domains with synchrotron radiation X-rays. *J Appl Crystallogr* **1999,** 32, (5), 841-849.
28. Brasen, D.; Wang, T., Pole Figure Measurements of Drawn and Rolled PVF2 Films. *J. Appl. Phys.* **1981,** 52, (9), 5543-5546.
29. Pazur, R.; Prud'Homme, R., X-ray Pole Figure and Small Angle Scattering Measurements on Tubular Blown Low-Density …. *Macromolecules* **1996**.
30. Salzmann, I.; Resel, R., STEREOPOLE: software for the analysis of X-ray diffraction pole figures with IDL. *Journal of Applied Crystallography* **2004,** 37, (6), 1029-1033.
31. Als-Nielsen, J.; McMorrow, D., *Elements of modern X-ray physics*. Wiley: New York, 2001.
32. Mannsfeld, S. C. B.; Virkar, A.; Reese, C.; Toney, M. F.; Bao, Z., Precise Structure of Pentacene Monolayers on Amorphous Silicon Oxide and Relation to Charge Transport. *Adv. Mater.* **2009,** 21, (22), 2294-+.
33. *This is not a rigorous requirement, but merely a guide. If the film is significantly thicker than the X-ray penetration depth, then only the surface region is probed*.
34. Breiby, D. W.; Bunk, O.; Andreasen, J. W.; Lemke, H. T.; Nielsen, M. M., Simulating X-ray diffraction of textured films. *Journal of Applied Crystallography* **2008,** 41, (2), 262-271.
35. Snyder, R. L.; Fiala, J.; Bunge, H. L., *Defect and Microstructure Analysis by Diffraction*. Oxford University Press: Oxford, **1999**.

36. Smilgies, D., Geometry-independent intensity correction factors for grazing-incidence diffraction. *Rev Sci Instrum* **2002,** 73, (4), 1706-1710.
37. Specht, E.; Walker, F., A Method for the Accurate Determination of Crystal Truncation Rod Intensities by X-ray Diffraction. *J Appl Crystallogr* **1993,** 26, 166-171.
38. Evans-Luetterodt, K.; Tang, M., Angle Calculations for a 2+2 Surface X-ray Diffractometer. *J Appl Crystallogr* **1995,** 28, 318-326.
39. Schleputz, C. M.; Herger, R.; Willmott, P. R.; Patterson, B. D.; Bunk, O.; Bronnimann, C.; Henrich, B.; Hulsen, G.; Eikenberry, E. F., Improved data acquisition in grazing-incidence X-ray scattering experiments using a pixel detector. *Acta Crystallographica Section A* **2005,** 61, (4), 418-425.
40. Warren, B. E., *X-Ray Diffraction*. Dover Publications, Inc.: New York, **1990**.
41. Barmak, K.; Kim, J.; Lewis, L. H.; Coffey, K. R.; Toney, M. F.; Kellock, A. J.; Thiele, J. U., On the relationship of magnetocrystalline anisotropy and stoichiometry in epitaxial L1[sub 0] CoPt (001) and FePt (001) thin films. *Journal of Applied Physics* **2005,** 98, (3), 033904-10.
42. Baker, J. L.; Widmer-Cooper, A.; Toney, M. F.; Geissler, P. L.; Alivisatos, A. P., Device scale vertical alignment of colloidal nanorods. *Nano Letters (submitted)* **2009**.
43. Huang, D.; Liao, F.; Molesa, S.; Redinger, D.; Subramanian, V. J., Plastic-compatible low resistance printable gold nanoparticle conductors for flexible electronics. *J Electrochem Soc* **2003,** 150, (7), G412-G417.
44. Faurie, D.; Renault, P. O.; Le Bourhis, E.; Goudeau, P., Study of texture effect on elastic properties of Au thin films by X-ray diffraction and in situ tensile testing. *Acta Materialia* **2006,** 54, (17), 4503-4513.